Optical Engineering

OpticalEngineering.SPIEDigitalLibrary.org

Microlaser assisted diamond turning of precision silicon optics

Hossein Shahinian
Jayesh Navare
Dmytro Zaytsev
Deepak Ravindra

SPIE.

Hossein Shahinian, Jayesh Navare, Dmytro Zaytsev, Deepak Ravindra, "Microlaser assisted diamond turning of precision silicon optics," *Opt. Eng*. **58**(9), 092607 (2019), doi: 10.1117/1.OE.58.9.092607.

Optical Engineering 58(9), 092607 (September 2019)

Microlaser assisted diamond turning of precision silicon optics

Hossein Shahinian,* **Jayesh Navare, Dmytro Zaytsev, and Deepak Ravindra**
Micro-LAM Inc., Portage, Michigan, United States

Abstract. The application of microlaser assisted machining of precision optical components made of optical grade single-crystal Si is reviewed. An optical raytracing model is developed and used for predicting the laser interaction with the workpiece. Optical characterization of the system is shown to be in good agreement with that predicted by the model. Using the information from the simulation and experimental validation, the laser-assisted diamond turning of single-crystal Si samples is shown to have exhibited little to no brittle fracture on the surface and the potential of extending the diamond tooling life by 150%. *© 2019 Society of Photo-Optical Instrumentation Engineers (SPIE)* [DOI: 10.1117/1.OE.58.9.092607]

Keywords: infrared optics; lasers; diamond turning.

Paper 190140SS received Jan. 29, 2019; accepted for publication Mar. 27, 2019; published online Apr. 11, 2019.

1 Introduction

The advent of ultraprecision machining (UPM) centers has been a significantly enabling technology in producing precise, optically smooth surfaces.[1] The key advantages of UPM are mainly the fast convergence and high determinism of the process.[2] Additionally, manufacturing complex free-form and aspherical optical components is far more convenient using UPM than that of traditional manufacturing techniques, i.e., grinding and polishing.[3] The primary limitation in using UPM is the limited number of materials that can be classified as machinable with such technologies.[4]

The machinability refers to the ability of UPM in achieving optically smooth surfaces (roughness values <10 nm RMS), with small figure errors (smaller than 50 nm root mean square irregularity). Typically, single-crystal diamond tools are used, as diamond is the hardest material, offering the most robust tool. The tool is machined with a very well-defined cutting edge, combined with the application of a high degree of thermal stability during the process,[5] as well as isolation from external vibration sources, enabling the high-positional repeatability of the UPM.[6,7]

Although initially UPM of soft metals in single-point diamond turning (SPDT) configuration was considered a great breakthrough in the optical fabrication realm, more recently the SPDT of hard and brittle infrared (IR) materials has gained traction within the community. Of great interest is the machining of single-crystal silicon (Si) optics. Si has a relatively high index of refraction, and with transmission rates of over 60%, it provides a great opportunity in designing IR optical components.[8,9] The alternative to Si is the much more expensive germanium (Ge) optics. Si is both lighter and cheaper than Ge, as well as its higher hardness offers superior mechanical properties to that of Ge. Nevertheless, due to Si's lower fracture toughness to hardness ratio, machining fracture free surfaces poses a bigger challenge than Ge.[10,11] Typically, the fractured surface exhibits anisotropic surface finish on zones along the cleavage planes.[12,13] These zones can be indicative of highly deformed crystal grains underneath the surface and are detrimental to the optical performance and mechanical integrity of the optic.[14]

The other key challenge in machining Si is the much higher tool wear rates compared to those in machining Ge.[15] The wear rates are a function of the material hardness, process temperatures, and chemical composition of the workpiece in SPDT.[4] Although some have suggested the use of flooded coolants, this negatively impacts the final form achievable on the part.

Many articles have investigated the effect of various process parameters on promoting a ductile cutting regime on Si.[16–20] Most of these techniques lead to severe limitations on workpiece sizes achievable. In this paper, an alternative approach is used, that is, the application of a laser beam during SPDT and exactly at the cutting edge of the single-crystal diamond tool.

2 Summary of the μ-LAM Process

The microlaser assisted machining (μ-LAM) process leverages a laser emission beam at the cutting interface between tool and workpiece to facilitate a more ductile cutting regime.[21] The laser is directed through a series of optics, which can then pass through a polished optical surface or integrated lens on the back face of the diamond. The laser position can be finely adjusted and placed precisely at the diamond tool edge, as shown in Fig. 1.

The laser light is absorbed by the workpiece material by 60% of the total irradiance. The absorption of the laser causes the material to be heated locally. As outlined by many articles,[22] single-crystal Si exhibits thermal annealing for temperatures near 1000°C. That said the annealing temperature is much lower in the presence of high-pressure values (>10 GPa).[23] Given the small contact area between the cutting tool and the workpiece surface during SPDT, such pressures are common to attain.[24] Thus it is speculated that the laser heating under the high pressures of SPDT promotes the ductile cutting of Si by annealing the surface.[25]

The laser absorption and heating process are localized only to an area <300 μm^2 at the vicinity of the tool tip.

*Address all correspondence to Hossein Shahinian, E-mail: hossein.shahinian@micro-lam.com

0091-3286/2019/$25.00 © 2019 SPIE

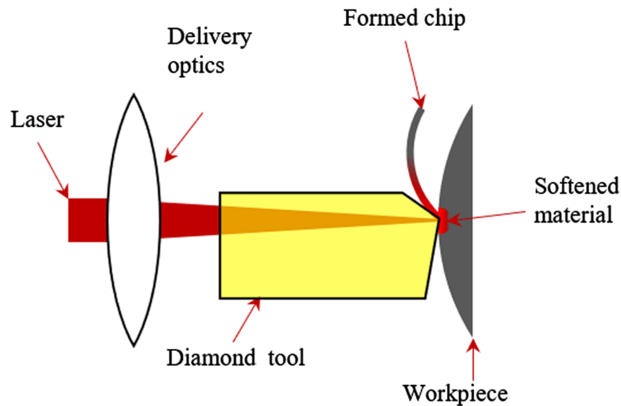

Fig. 1 Overview of μ-LAM process.

Therefore, there is no bulk heating of the material, and the heat introduced is then immediately dissipated in the chips of removed material. This localized heating is crucial in achieving the desirable form error of the surface.

The optical raytracing model from which the laser power and irradiance can be predicted were generated. The predictions were complimented by experimental measurements. Machining experiments were conducted to verify three aspects of the μ-LAM process: (1) the laser heating is localized and repeatable, (2) the laser heating does promote a higher degree of ductile cutting, and (3) the more ductile regime machining increases the tool life during machining.

3 Experimental Equipment

3.1 *Test Bed*

The testing was done on an ultraprecision lathe, a Precitech Nanoform 250 Ultra, see Fig. 2(a). The lathe consists of two computerized numerically controlled axes, X and Z (both have a travel range of 220 mm), as well as an active hydraulic damping system to minimize the vibrations induced during the machining. The workpiece was mounted to an HS-150 high-speed air bearing spindle. The spindle had a maximum RPM of 15,000. The positional repeatability of the machine was <10 nm.

A custom-made toolpost, the Optimus, was affixed to the machine table as depicted in Fig. 2(b). The toolpost consists of a rigid tool holder and a carriage that holds the laser delivery optical system (LDOS). The LDOS was comprised of a collimator and a series of optical elements, see Fig. 3, directing the laser toward the cutting edge of the diamond tool. The carriage also incorporates micrometers that allow the proper calibration and alignment of the laser beam position with respect to the tool. The tool holder used a differential screw mechanism to align the tool to the centerline of the spindle. The laser beam was produced in an Nd:YAG lasing medium with a wavelength of 1064 nm (IR beam). In addition, a low-power, visible, HeNe laser (red beam) was also incorporated, concentered with the Nd:YAG laser beam, for alignment purposes. The complete module was controlled with the laser control station (LCS) depicted in Fig. 2(a). The LCS had the ability of changing the IR beam power by 1-W increments.

3.1.1 *Diamond tools*

The tools were made of single-crystal synthetic high-pressure, high-temperature diamond material. The μ-LAM process used a proprietary tool design that allowed the transmission of laser light through the tool, thereby irradiating the cutting interface. The diamond tool is described by its nose radius (the radius of curvature of the cutting edge), the rake angle, and the clearance angle, as shown in Fig. 3. The tools used in the experiment had nose radius of 0.3 mm, rake angle of −35 deg, clearance angle of 10 deg, and a cutting height (see Fig. 3 for cutting height) of 0.9 to 1.0 mm.

3.1.2 *Laser beam alignment*

To ascertain that the cutting interface received the proper amount of laser power and that the laser was emitting through the proper region of the tool, an alignment procedure was performed. The alignment equipment consists of a multispectral absorbing power meter and a camera imaging the aperture of the power meter, see Fig. 4(a). The low-power, visible red beam was used to align the beam laterally. The vertical alignment of the beam was performed by measuring the power coming through the diamond and adjusting the vertical micrometer to a spot that the central zone of the beam was near the cutting edge. The beam was aligned to output 30% to 50% of its total power through the clearance face of the diamond tool. It is speculated that this ratio produces a more uniform distribution of the laser power along the cutting edge of the tool. For the cutting experiments

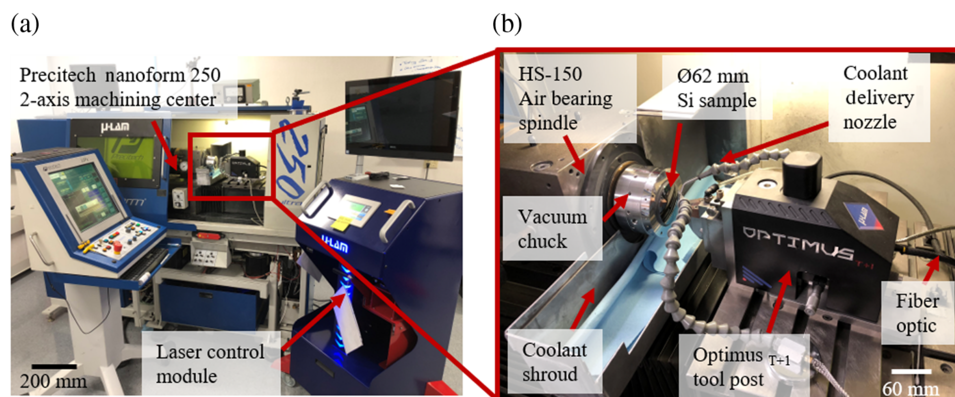

Fig. 2 Experimental setup: (a) LCS integrated with Precitech two-axis machining center and (b) test bed with Optimus toolpost and Si sample.

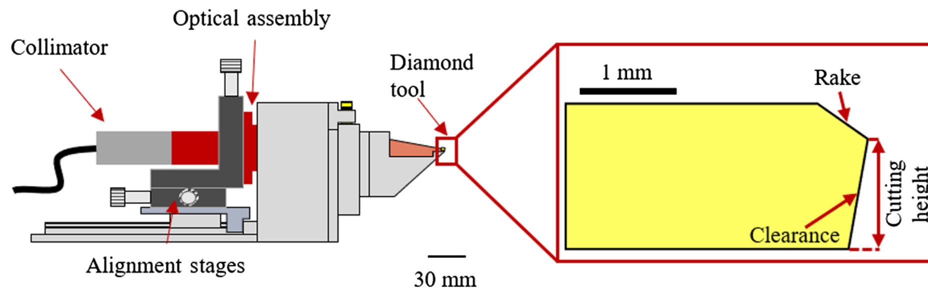

Fig. 3 Optimus toolpost and diamond tool schematic.

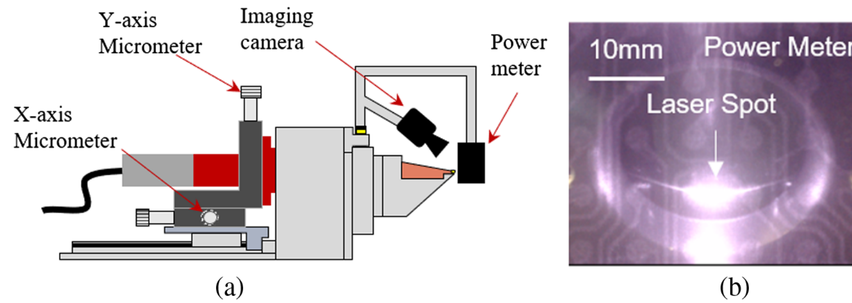

Fig. 4 (a) Laser alignment accessory and (b) image of laser spot on power meter.

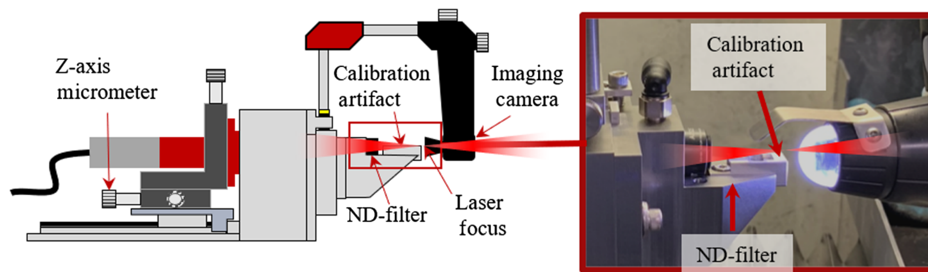

Fig. 5 Laser spot calibration equipment and procedure.

reported in this paper, the power measured through the clearance was 2.7 W. Fig. 4(b) depicts the image of the IR beam spot on the power meter.

3.1.3 *Laser spot calibration*

To ensure the repeatability of the delivered laser beam at the tool tip, a calibration procedure was used. A shallow depth of field imaging camera was mounted to the toolpost and focused onto a calibration artifact that was placed onto the front of the toolpost, see Fig. 5. This artifact represents a known position relative to the nominal diamond tool cutting edge, whereby the camera was focused on. The red beam, imaged by the same camera, was then moved axially such that a minimum spot size was attained. The axial motion of the beam is provided by the Z axis micrometer shown in Fig. 5.

3.2 *Test Sample*

The sample used for the testing was a ∅62 mm plano-convex single-crystal Si optic. The crystal lattice had $\langle 111 \rangle$ direction. The radius of curvature of the part was 205 mm. The sample was diamond turned prior to the commencement of the testing to ensure that the surface was free of tilt, grinding marks, and any other defects.

3.3 *Metrology*

The Si sample was subjected to two types of surface metrology, i.e., form and surface finish measurements. The form measurements were taken on a Taylor Hobson LuphosScan® 260 HD, a noncontact multiwavelength scanning interferometer. The surface finish measurements were taken using a Taylor Hobson coherence correlation interferometer (CCI). The metrics and data processing used for evaluation of form and surface finish measurements are listed in Table 1.

4 Raytracing Model

The raytracing model was created in Zemax OpticStudio®. Both sequential and nonsequential raytracings were used.

4.1 *Sequential Raytracing*

The sequential module was used for prediction of the focusing spot size of the LDOS. Figure 6(a) shows the overall layout of the optical system used in the Optimus toolpost. In Fig. 6(b), the focusing spot is calculated to be as much as 20.94 μm.

Table 1 Metrology equipment and metrics.

Instrument	Metrics and processing parameters
Taylor Hobson CCI	Surface roughness measurement, fourth-order Chebyshev removed, high-pass filter with $\lambda_c = 0.08$ mm
	Metrics: RMS roughness, *Sq* (nm)
LuphosScan 260 HD	Form measurement, piston, tilt, and power removed
	Metrics: peak-to-valley (μm)

4.2 *Nonsequential Raytracing*

The nonsequential module is used to predict and study the exiting beam from the tip of the diamond tool and to gain more realistic data for machining purposes. The beam was modeled as a Gaussian beam, with beam divergence of 24.5 mrad, and a beam waist size of 24 μm. The diamond tool geometry was generated in SolidWorks® and imported to Zemax®. A total of 10^6 number of analysis rays were used. Due to the curved shape of the tool tip, a surface detector with the same curvature of the diamond tool was used. The detector had 300 radial and 300 angular zones.

5 Optical Characterization Test Bench

5.1 *LDOS Evaluation*

To verify the calculations from the raytracing model, measurements of the laser beam at the exit of the LDOS were conducted. The measurements were done using a Thorlabs BP104-UV beam profiler. The beam profiler has a high sensitivity to laser beams with wavelength between 200 to 1100 nm.[26] To characterize the spot size, the full-width half-maximum (FWHM) of the beam profile in two perpendicular orientations was measured. Figure 7(a) illustrates the measurement setup. The beam profiler can tolerate power densities up to 10 kW/cm^2 for a spot size of $\sim$30 μm. Due to the expected high-power densities of the delivered laser beam ($>$160 kW/cm^2), a beam splitter was used to reduce the laser power at the beam profiler aperture by 95%. The beam profiler was traversed along the X axis near the focal point of the optical system for 10 mm of total travel length.

At each measurement point, the FWHM of the Gaussian beam was calculated. Figure 7(b) shows the FWHM values of the beam in the two perpendicular directions. The spot was minimum at 105 mm away from the last surface of the focusing system and the focus spot was $\sim$25.86 μm. These measurements were repeated over 6 times and the standard deviation of the measurement was less than 0.5 μm. The theoretical model underpredicted the experimental measurements by 5 μm. This good agreement between the model and the experimental measurement gave credibility to future predictions and designs using the raytracing approach.

5.2 *Beam Delivery Through the Diamond Tool*

The key element of the μ-LAM process is the delivery of the IR laser beam at the tip of the diamond tool. The diamond tool is optically transparent and absorbs the laser by $\sim$30%. Furthermore, the beam is defocused, and the spot size was $\sim$240 μm at the cutting of the tool, see Fig. 8(a).

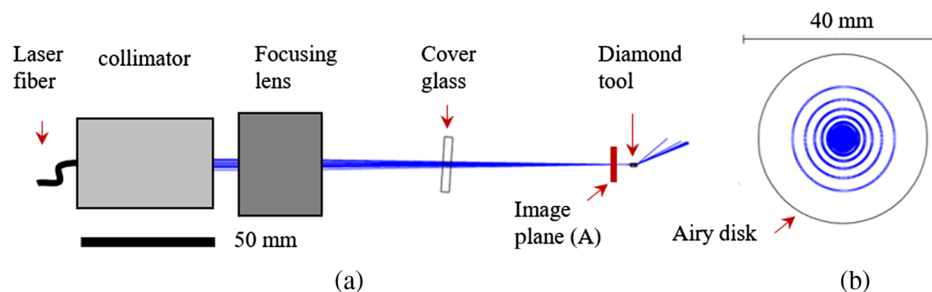

Fig. 6 Raytracing model of the μ-LAM optical system: (a) system layout and (b) image of the spot at image plane (A) using sequential raytracing.

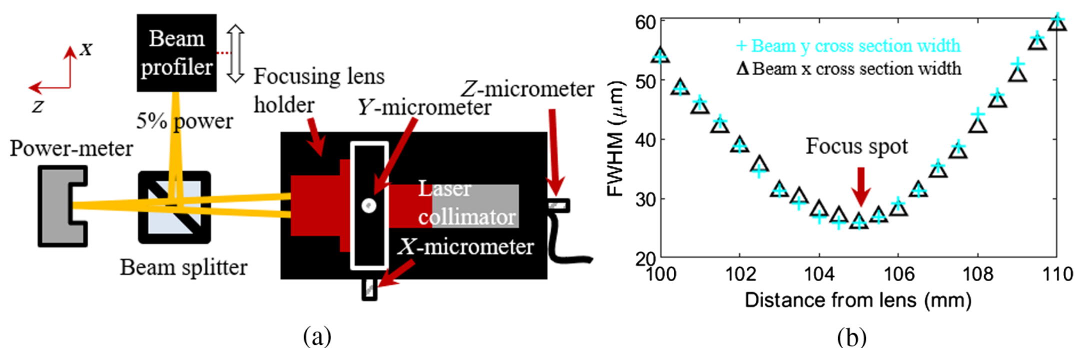

Fig. 7 Focus spot measurements: (a) schematic of the test benchmark and (b) spot measurements over 10 mm.

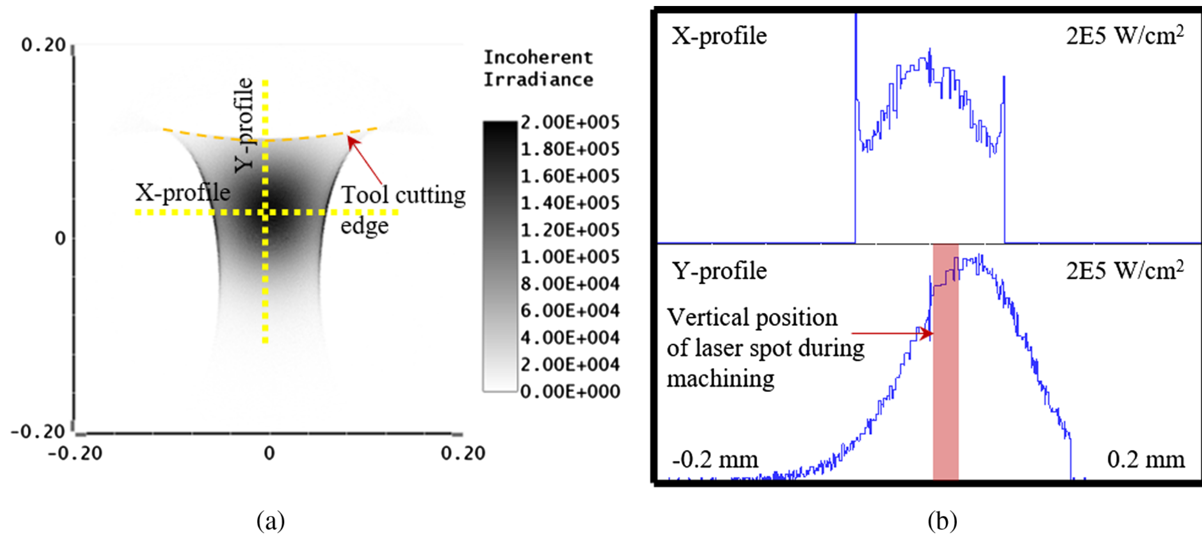

Fig. 8 (a) 3-D contour map of laser spot exiting the clearance face and (b) linear profiles from the laser spot.

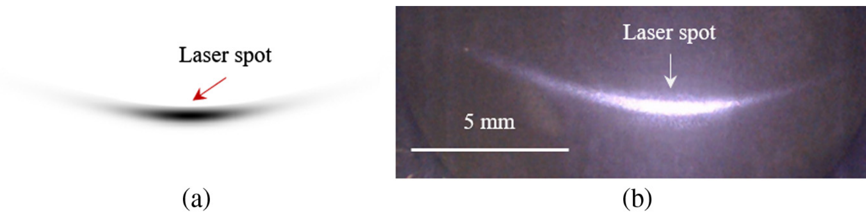

Fig. 9 Laser spot 5 mm away from diamond tool: simulation from (a) Zemax and (b) real image.

Figure 8(b) shows linear profiles extracted from the laser spot. The laser spot shows the Gaussian nature of the beam in both cross sections. The red highlighted zone in the Y profile marks the laser beam profile during machining near the cutting edge of the tool.

To verify the predicted spot size by the raytracing model, the shape and size of the laser beam 5 mm away from the tool tip is evaluated. This position corresponds to the image plane of the laser power-meter outlined in Sec. 3.1.3. Figures 9(a) and (b) depict the laser spot from the raytracing model and that imaged on the laser power-meter, respectively. Evidently, the spot from the model and that measured are in very good agreement.

6 Diamond Turning of Si

To evaluate the cutting performance of the μ-LAM process, three metrics were investigated: (1) how does the process influence form errors on single-crystal Si, (2) what is the surface finish of the workpiece produced using μ-LAM, and (3) what is the impact of the process on overall tool life.

6.1 *Testing Conditions*

6.1.1 *Test group A: surface form and finish*

To study the effect of μ-LAM process on the form and surface finish, UPM of single-crystal Si using conventional SPDT and μ-LAM was done. The tests involved two machining passes (cuts) where the first cut used a tool path to generate the desired convex geometry and the second cut used a compensated tool path to account for the surface errors measured after the first cut. The machining parameters were selected based on the information available in the literature[10] and are listed in Table 2.

6.1.2 *Test group B: tool wear analysis*

To quantify tool life, SPDT of the Si sample with and without μ-LAM was done in sequential passes, to the point where brittle fracture zones on the cleavage planes appeared on the surface. The total track length travelled by the tool up to the end of the pass prior to the appearance of the fracture zones was deemed as the tool life.

Table 2 Test conditions for analyzing form and surface finish.

Test	Tool	Laser power (W)	RPM	Feed (mm/min)	Depth of cut (μm)	Coolant (mist)
Si-1	0.3 mm, −35-deg rake, 10-deg clearance	0	2000	3	6	Odorless mineral spirits (OMS)
Si-2	0.3 mm, −35-deg rake, 10-deg clearance	2.7	2000	3	6	OMS

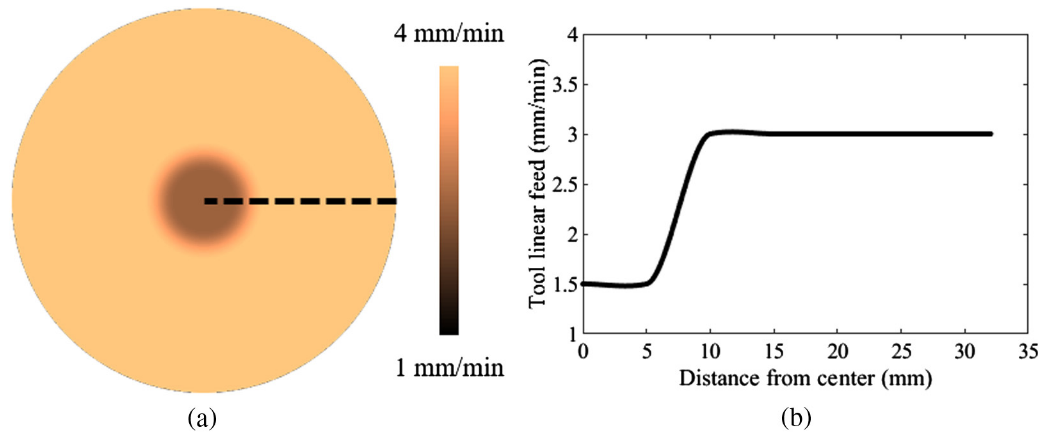

Fig. 10 Variable feed rate view graphs: (a) 3-D view and (b) 2-D slice on the dashed line.

A total of five diamond tools were used and all tools underwent the SPDT of the Si sample with and without μ-LAM. The machining parameters were similar to that listed in Table 2 with the exception of the linear feed rate. A variable feed rate starting with 3 mm/ min near the outer edge and gradual reduction to 1.5 mm/ min at the center. The reason for this variable feed is that the 3 mm/ min feed caused the appearance of zones of brittle fracture near the center and the lower 1.5 mm/ min mitigates the zones to a great extent. Figure 10(a) depicts the velocity gradient map of the tool, whereas Fig. 10(b) shows a linear slice of the 3-D map.

6.2 *Machining Results*

6.2.1 *Form measurements: test group A*

Figures 11(a) and 11(b) depict the form error induced on the Si sample using conventional SPDT and μ-LAM, respectively. The measurement is taken after the compensated tool path was used. From Fig. 11, it is observed that the form errors imparted on the Si sample by conventional SPDT and the μ-LAM process are similar. The large astigmatism errors present in the measurements are due to the high-vacuum chuck pressure holding the parts during machining.

The results demonstrate that the addition of the laser source during machining Si was not an impeding factor in achieving form errors expected in UPM. The concern was that the addition of a heat source, i.e., the laser power, would induce thermal gradients that would effectively eliminate the process determinism of UPM. This is not the case for two main reasons: (1) the heat effect under controlled conditions was very repeatable and (2) the heated zone was highly localized and was only near the cutting edge.

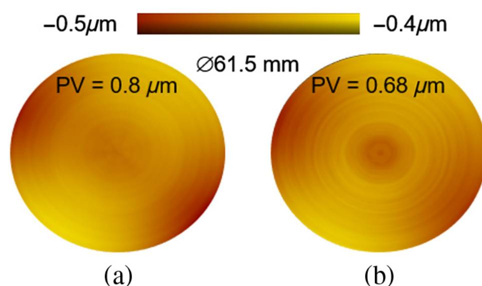

Fig. 11 Form error measurements on Si sample: (a) conventional diamond turning and (b) μ-LAM process.

6.2.2 *Surface roughness measurements: test group A*

Figures 12(a) and 12(b) depict the areal map of roughness measurements near the center of the same Si sample machined with and without μ-LAM, whereas Figs. 12(c) and 12(d) show off-centric areal maps of the same samples. The near-center interferogram of the sample machined with conventional SPDT shows clear signs of brittle fracture zones, whereas such zones are greatly minimized with the addition of μ-LAM.

The RMS roughness Sq is reported in Fig. 12 as well. The surface roughness values for both processes, match closely in the off-center regions. The roughness measurements in other areas of the part (apart from the center) are similar to that shown in Figs. 12(c), 12(d). The roughness values have improved by a factor of 5 near the center using μ-LAM. This improvement is primarily due to the disappearance of the brittle fracture zones.

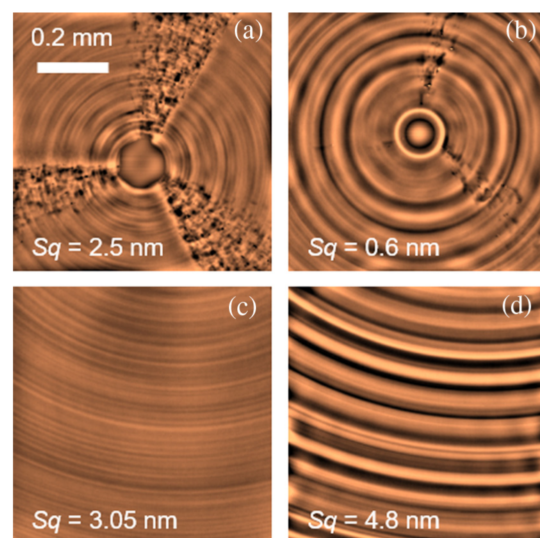

Fig. 12 Roughness measurement on Si sample: (a) near center with conventional diamond turning, (b) near center with μ-LAM process, (c) off-center with conventional diamond turning, and (d) off-center with μ-LAM process.

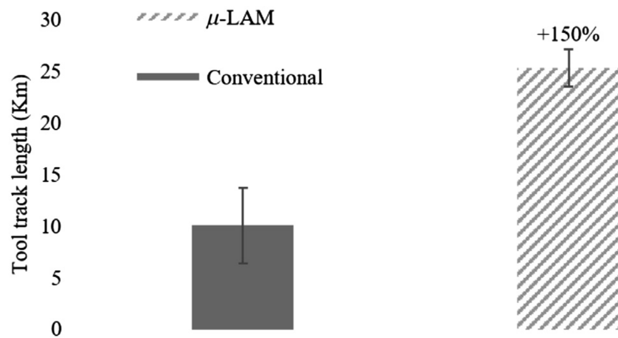

Fig. 13 Tool track length for Si sample machined with conventional SPDT and the μ-LAM process.

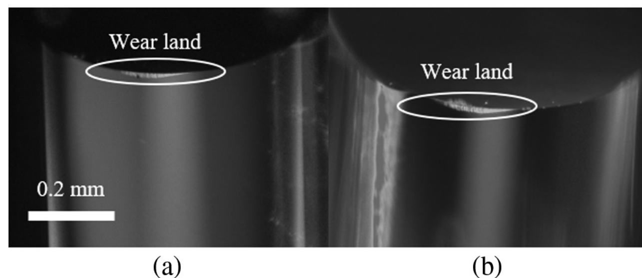

Fig. 14 Microscopic image of tool wear land: (a) conventional SPDT and (b) μ-LAM.

6.2.3 *Tool wear: test group B*

Figure 13 depicts the total track length covered by the tool in accordance with the criteria described in Sec. 6.1.2.

The results in Fig. 13 show 150% increase in tool life with the addition of μ-LAM. As mentioned earlier, these results are obtained with five different tools with similar materials and geometries. The evidentiary increase in tool life, combined with the observation of less brittle fracture zones, strongly suggest that the laser heating effect does indeed promote ductile machining of brittle Si. It is speculated that the highly focused laser spot potentially increases the temperature of the cutting zone by 500°C to 600°C, and thus causing a phase change to the Si surface under enormous cutting pressures.

Figure 14 shows the worn tools post SPDT of the Si sample. The wear patterns induced by conventional SPDT [Fig. 14(a)], closely matches that induced by μ-LAM [Fig. 14(b)]. The tool used in conventional SPDT shows small isolated defects on the cutting edge, whereas the tool machined with μ-LAM displays zones that are abraded uniformly, and no obvious defects can be seen. It is suspected that the harder surface material during conventional SPDT has caused the localized fractures to the tool tip, manifesting itself in the form of the defects.

7 Conclusions and Future Work

In this paper, commercial SPDT of single-crystal Si using the μ-LAM process was demonstrated. They key highlights of the paper can be summarized as the following:

- μ-LAM introduces very localized and efficient heating of the surface being cut and does not complicate the process determinism of SPDT with the addition of the heat source.
- μ-LAM shows a higher level of ductile machining of single-crystal Si, confirmed by the existence of little to no brittle fracture zones and longer tool life.
- The optical simulation results can be used as a future predictive model for process performance.

As future efforts to further investigate the dominant mechanism during μ-LAM of optical components, cutting load measurements, and the effect of the laser on forces will be investigated. Furthermore, x-ray diffraction measurements of Si samples under pressure and emission of the laser beam will be pursued. It is believed that the proposed methods will provide a comprehensive set of evidence verifying the removal mechanisms outlined in this article. Such studies will not be limited to Si and additional hard to machine materials will also be studied.

Acknowledgments

We would like to thank the National Science Foundation (NSF) for providing funding (Award no. IIP-1330439), and the entire Micro-LAM team for their support in doing this project.

References

1. T. T. Saito, "Diamond turning of optics: the past, the present, and the exciting future," *Opt. Eng.* **17**(6), 176570 (1978).
2. M. A. Davies et al., "Application of precision diamond machining to the manufacture of microphotonics components," *Proc. SPIE* **5183**, 94–108 (2003).
3. F. Fang et al., "Manufacturing and measurement of freeform optics," *CIRP Ann.* **62**(2), 823–846 (2013).
4. E. Paul et al., "Chemical aspects of tool wear in single point diamond turning," *Precis. Eng.* **18**(1), 4–19 (1996).
5. J. Bryan, "International status of thermal error research (1990)," *CIRP Ann. Manuf. Technol.* **39**(2), 645–656 (1990).
6. J. B. Bryan, "Design and construction of an ultraprecision 84 inch diamond turning machine," *Precis. Eng.* **1**(1), 13–17 (1979).
7. T. T. Saito, "Diamond turning of optics," *Opt. Eng.* **15**(5), 155431 (1976).
8. Y. Su et al., "Analysis and discussion on processing and adjusting technology of infrared optical system," *Proc. SPIE* **10838**, 1083816 (2019).
9. G. Kintz and P. Stephanou, "Wide bandwidth, achromatic, planar silicon lenses for long-wave infrared imaging," *Proc. SPIE* **10627**, 1062709 (2018).
10. S. S. To, V. H. Wang, and W. B. Lee, *Machinability of single crystals in diamond turning, in Materials Characterisation and Mechanism of Micro-Cutting in Ultra-Precision Diamond Turning*, Springer, Berlin Heidelberg, pp. 43–69 (2018).
11. L. N. Abdulkadir et al., "Ultra-precision diamond turning of optical silicon—a review," *Int. J. Adv. Manuf. Technol.* **96**, 173–208 (2018).
12. T. Nakasuji et al., "Diamond turning of brittle materials for optical components," *CIRP Ann. Manuf. Technol.* **39**(1), 89–92 (1990).
13. T. Shibata et al., "Ductile-regime turning mechanism of single-crystal silicon," *Precis. Eng.* **18**(2–3), 129–137 (1996).
14. J. Yan et al., "Fundamental investigation of subsurface damage in single crystalline silicon caused by diamond machining," *Precis. Eng.* **33**(4), 378–386 (2009).
15. J. Yan, K. Syoji, and J. I. Tamaki, "Some observations on the wear of diamond tools in ultra-precision cutting of single-crystal silicon," *Wear* **255**(7–12), 1380–1387 (2003).
16. M. Heidari, J. Akbari, and J. Yan, "Effects of tool rake angle and tool nose radius on surface quality of ultraprecision diamond-turned porous silicon," *J. Manuf. Processes* **37**, 321–331 (2019).
17. Y. Karpat, "Influence of diamond tool chamfer angle on surface integrity in ultra-precision turning of singe crystal silicon," *Int. J. Adv. Manuf. Technol.* **101**(5–8), 1565–1572 (2019).
18. N. Khatri et al., "An experimental investigation on the influence of machining parameters on surface finish in diamond turning of silicon optics," *Proc. SPIE* **9654**, 96540M (2015).
19. D. Huo, *Micro-cutting: Fundamentals and Applications*, John Wiley & Sons, Hoboken, New Jersey (2013).
20. C. Wang et al., "Cutting force-based analysis and correlative observations on the tool wear in diamond turning of single-crystal silicon," *Proc. Inst. Mech. Eng. Part B: J. Eng. Manuf.* **229**(10), 1867–1873 (2015).
21. D. Ravindra, "Ductile mode material removal of ceramics and semiconductors," Western Michigan University, Volume 73-05 Section B: p338 (2011).

22. N. Ookubo et al., “Effects of thermal annealing on porous silicon photoluminescence dynamics,” *Appl. Phys. Lett.* **61**(8), 940–942 (1992).
23. M. Kaczmarski, O. N. Bedoya-Martinez, and E. R. Hernández, “Phase diagram of silicon from atomistic simulations,” *Phys. Rev. Lett.* **94**(9), 095701 (2005).
24. A. Mir, X. Luo, and J. Sun, “The investigation of influence of tool wear on ductile to brittle transition in single point diamond turning of silicon,” *Wear* **364**, 233–243 (2016).
25. D. Ravindra, M. K. Ghantasala, and J. Patten, “Ductile mode material removal and high-pressure phase transformation in silicon during micro-laser assisted machining,” *Precis. Eng.* **36**(2), 364–367 (2012).
26. Thorlabs, *Thorlabs Beam Beam Analyzing Software BP104-UV, -VIS, -IR, -IR2, BP109-UV, -VIS, -IR, -IR2, Operational Manual*, Thorlabs, Inc., Newton, New Jersey (2011).

Biographies of the authors are not available.